Shear Transformation Zone Dynamics Modeling of Deformation in Metallic Glasses

56

Lin Li and Eric R. Homer

Contents

Abstract

A mesoscale shear transformation zone (STZ) dynamics model is presented to investigate the deformation behaviors of metallic glasses that span significant time and length scales. The modeling framework involves coarse-graining STZs, the fundamental deformation unit in metallic glasses, onto a finite element mesh and controlling the stochastic activation of these STZs using the kinetic Monte Carlo algorithm based on the energetics of the glass system. The combination of these two features allows simulating diverse deformation modes of metallic

L. Li (✉)
Department of Metallurgical and Materials Engineering, The University of Alabama, Tuscaloosa, AL, USA
e-mail: lin.li@eng.ua.edu

E. R. Homer
Department of Mechanical Engineering, Brigham Young University, Provo, UT, USA
e-mail: eric.homer@byu.edu

W. Andreoni, S. Yip (eds.), *Handbook of Materials Modeling*,
https://doi.org/10.1007/978-3-319-44677-6_99

glasses at large time and length scales while providing a microscopic view of the process that dominates the behaviors. The adaption of the STZ dynamics framework to treat complex phenomena is discussed, including a detailed examination of the shear banding process, simulated contact mechanics, and an examination of the interplay of deformation and structural evolution via the incorporation of a free volume state variable. The chapter concludes with the challenges and future development of the STZ dynamics model.

1 Introduction

Metallic glasses exhibit deformation behaviors that are both interesting and challenging to fully characterize. As a result, a complete understanding of this new class of materials requires modeling techniques that can capture the relevant phenomena at the appropriate scales (Rodney et al. 2011; Schuh et al. 2007). The amorphous structures of metallic glasses appear deceptively homogeneous and isotropic when investigated with conventional experimental characterization techniques; the materials don't exhibit typical defect structures, such as dislocation, present in crystalline alloys. Despite the lack of experimental means to directly characterize flow defects, the state of the art in material modeling offers highly accurate methods, from density functional theory and molecular dynamics at atomistic scales all the way up to continuum theories for the deformation of metallic glasses and its connection with amorphous structures.

The deformation of metallic glasses, in particular, the low-temperature shear banding behavior is a typical multiscale phenomenon (Greer et al. 2013), occurring over several length and time scales illustrated in Fig. 1. At the atomic scale, the fundamental units of deformation are atomic rearrangements called shear transformation zones (STZs) (Argon 1979). The STZs are localized both in space, involving only a few tens of atoms, and time, spanning a few picoseconds, which have been captured and extensively studied by atomistic simulations (Falk and Maloney 2010; Rodney et al. 2011). The structural origin of STZs remains elusive, and yet it is believed that the inhomogeneous atomic packing configurations in the amorphous structure lead to a heterogeneous local inelastic response, linking to STZs (Cheng and Ma 2011; Ma and Ding 2016). Figure 1e displays a reconstructed atomic configuration of $Zr_{50}Cu_{45}Al_5$ metallic glasses by hybrid reverse Monte Carlo simulation, revealing a variety of packing clusters including the ideal icosahedron, distorted icosahedron, and face-centered cubic structure. Using molecular dynamics simulations, Ding et al. demonstrate that the regions densely populated with unstable clusters are elastically soft and more susceptible to be STZs (Fig. 1f). Such nanoscale inelastic heterogeneities have been recorded experimentally using dynamic atomic force microscopy (Fig.1b) and nanoindentation (Fig.1c). At the mesoscopic scale, the collective behaviors of STZs lead to various unique deformation phenomena in amorphous materials, such as spontaneous strain localization/shear banding, intermittent dynamics, and power-law distributed avalanches, which receive considerable attention from mesoscale modeling and experiments (Dahmen et al. 2009; Rodney et al. 2011). The connection of these deformation

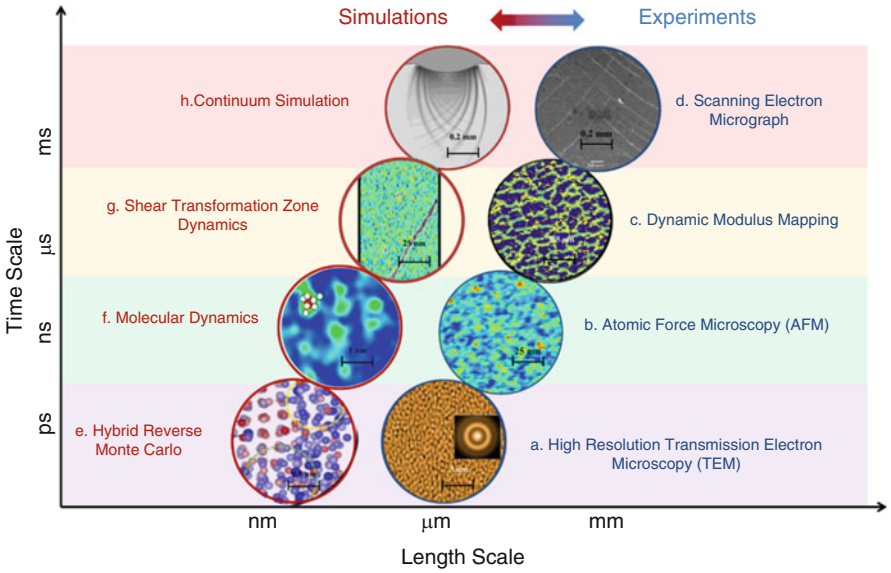

Fig. 1 Multiscale features of the deformation behaviors and structural heterogeneities in metallic glasses. (**a**) The disordered atomic structure imaged by high-resolution transmission electron microscopy (HRTEM) (Ma and Zhang 2010). (**b**) The inelastic phase shift image of $Zr_{55}Cu_{30}Ni_5Al_{10}$ metallic glass with a correlation length ~5 nm using atomic force microscopy (AFM) (Liu et al. 2011). (**c**) The elastic microstructure of $Zr_{58.5}Cu_{15.6}Ni_{12.8}Al_{10.3}Nb_{2.8}$ metallic glass with a characteristic length ~100 nm characterized by dynamic modulus mapping on nanoindentation platform (Tsai et al. 2017). (**d**) Intersecting shear bands under the indenter of a Zr-based MG using scanning electron microscopy (SEM) (Su and Anand 2006). (**e**) The reconstructed atomic clusters of $Zr_{50}Cu_{45}Al_5$ MG by hybrid reverse Monte Carlo simulations (Hwang et al. 2012). (**f**) The atoms experienced shear transformation overlap on the participation ratio of soft modes in a $Cu_{64}Zr_{36}$ MG obtained by molecular dynamics (MD) simulations (Ding et al. 2014). (**g**) The simulated shear band formation of a $Cu_{64}Zr_{36}$ MG in the presence of elastic heterogeneity using a mesoscale shear transformation zone (STZ) dynamics simulations (Wang et al. 2018). (**h**) Simulated shear band pattern under indentation using a continuum model (Su and Anand 2006)

behaviors to the amorphous structure is beyond short-range orders; the atomic heterogeneities coordinate over a larger scale, translating from the nanometer-scale STZs to their organization into shear bands (Fig. 1g), which usually appear within a few milliseconds and reach a length on the order of a tenth of a micrometer. Finally, at the macroscopic scale, depending on the loading condition, either a single shear band forms as in tension test, or several shear bands form and interact, in case of confined plasticity as in indentation tests, as shown in Fig. 1d, h. The continuum modeling of the deformation behavior of metallic glasses has mostly relied on a flow rule accounting for the evolution of an internal state variable, the free volume, proposed by Spaepen (1977), relating the plastic strain rate to the state of stress and the history of deformation of the glass.

On the modeling front, atomistic simulations are critical in resolving the physics and mechanics associated with individual STZ activations, the nature of STZ-STZ interactions (Falk and Maloney 2010) as well as the incipient stage of shear band

nucleation (Şopu et al. 2017). Unfortunately, the atomistic simulations limit in both time and length scale to simulate the shear banding behaviors at engineering scales. Continuum approaches, on the other hand, can model deformation at engineering scales and provide an ideal comparison to experiments (Su and Anand 2006). However, the presumed constitutive laws can only exhibit phenomena they have been designed to capture, and often the deformation physics that must be introduced is not completely understood. As a result, a mesoscale modeling technique is an important inclusion in modeling the deformation behavior of metallic glasses across the entire spectrum (Rodney et al. 2011), contributing toward a complete understanding of structure-mechanical property relationships in metallic glasses (Hufnagel et al. 2016).

Modeling the amorphous plasticity at the mesoscopic scale, one employs a coarse-grained description of the STZs and accounts for the dynamics of these elementary STZ processes; by averaging out atomistic effects, one can access larger scales in the same way as dislocation dynamics describes crystal plasticity. Rodney et al. have summarized the key ingredients of mesoscale models for amorphous materials, which include a local activation/yield criterion of STZs, an elastic coupling between STZ and amorphous matrix like an Eshelby inclusion, the evolution rule of activation/yield criterion, and a dynamical rule that associates a time scale to the STZ activations (Rodney et al. 2011). Based on the different choices of these rules, the mesoscale models for metallic glasses fall into three categories. First, a depinning model, developed by Vandembroucq et al. (Baret et al. 2002), employs statistical distributions of yield stresses as well as the transformation strains for STZs, driving the evolution of STZs via internal stress arising from the accumulation of Eshelby fields and extremal dynamics. Second, a fluidity model, developed by Picard et al. (2002), uses a constant yield-stress criterion for STZs and incorporates the glassy dynamics based on Maxwellian viscosity through a distribution of characteristic transition rates. Third, an STZ dynamics model (Bulatov and Argon 1994a; Homer and Schuh 2009; Zhao et al. 2013), which is the focus of this chapter, uses an energy-based activation criterion for the STZs and a kinetic Monte Carlo algorithm to evolve the system through Boltzmann statistics.

In this chapter, we discuss the development of the STZ dynamics modeling framework and its applications in various aspects of metallic glass deformation, detailing the techniques used to bridge the relevant time and length scales. In addition, we examine the deformation physics elucidated by this method as well as the mechanics associated with shear banding behaviors.

2 STZ Dynamics Modeling Framework

The mesoscale STZ dynamics model treats STZs as the elementary deformation events, and the stochastic activation of the STZs leads to the formation of shear bands at large time and length scales (Homer et al. 2010; Homer and Schuh 2009). This initial development of STZ dynamics framework is inspired by the work of Bulatov and Argon (1994a, b, c). As with Bulatov, the modeling framework

employs two separate elements, coarse-graining and kinetic Monte Carlo (kMC) algorithm, which individually bridge the length and the time scales associated with deformation in metallic glasses. The coarse-graining method centers on the STZ, which consists of a cluster of atoms that exhibit the transient shearing motion consistently in the same manner (Maloney and Lemaître 2004, 2006; Rodney and Schuh 2009; Srolovitz et al. 1983). Then a simulated metallic glass is represented by a system of potential STZs. The coarse-graining enables more efficient sampling of larger system sizes. Meanwhile, to simulate longer system times more efficiently, the transient STZ activation is considered as a transition state between the initial and final equilibrium configurations. Thus, transition state theory (TST) and the kMC algorithm can be employed as long as knowledge of the energetic landscape, including the transition states, is available.

2.1 STZ Coarse-Graining with Finite Element Mesh

The STZ coarse-graining is accomplished by replacing the cluster of atoms that represents a potential STZ with a feature of finite element mesh, as illustrated in Fig. 2 (Homer and Schuh 2010, 2009). In this process, three criteria are imposed for proper representation of an STZ using a finite element mesh. First, the coarse-grain representation should approximate the shape of an STZ, which is believed to be roughly spherical. Second, the finite element representation of the potential STZs should allow them to overlap, since the STZ is a transient event and the atoms involved would never be restricted to participate in only one potential STZs. In other words, for a given element, it can participate in multiple STZ activations. Third, the coarse-grained STZ should accurately capture the analytical solution of an Eshelby inclusion (Eshelby 1957). This is supported by the original STZ theory paper, in which Argon modeled the STZ as an Eshelby inclusion (Argon 1979).

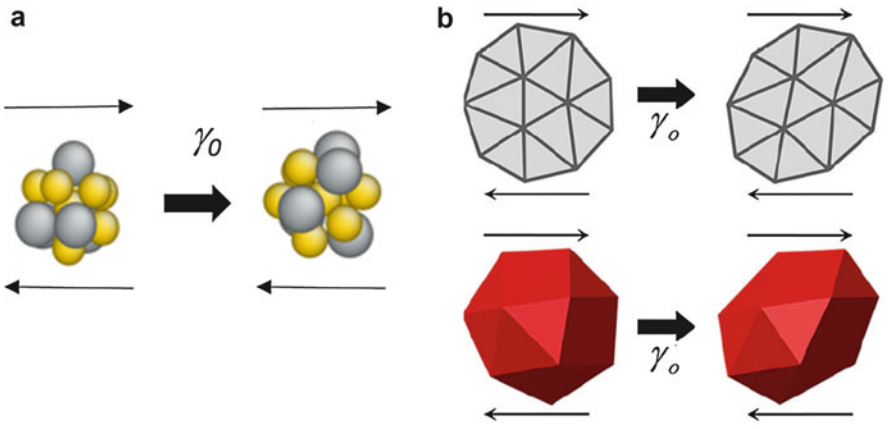

Fig. 2 Coarse-graining of an STZ (**a**) using features of a finite element mesh in (**b**) 2D or 3D. (Figure adapted with permission from Homer and Schuh (2009, 2010))

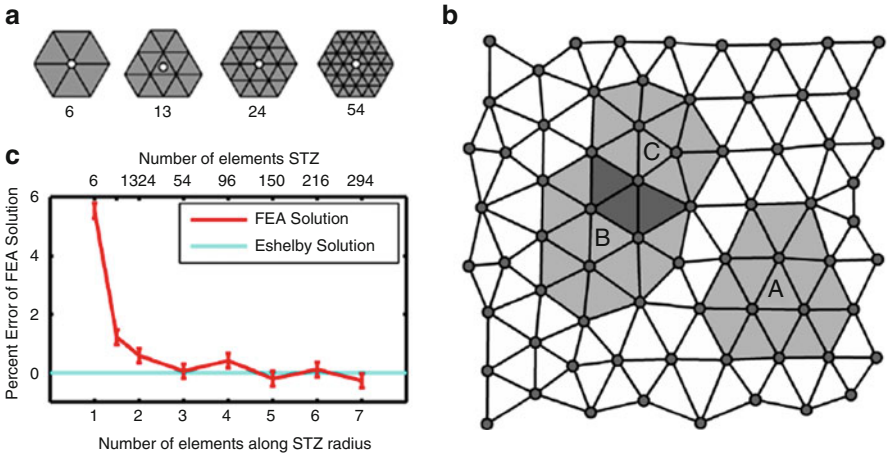

Fig. 3 2D coarse-graining process. (**a**) Representation of possible STZ definition on the triangular mesh. (**b**) Irregular triangular mesh with 13-element potential STZs highlighted to show how the individual elements in the mesh can be activated by different STZs. (**c**) The accuracy of STZ coarse-graining evaluated by the strain energy difference between finite element method and the Eshelby solution as a function of the size of the STZ (Figure adapted with permission from Homer and Schuh (2009))

Following the three criteria, the implementation of coarse-graining STZs onto 2D and 3D finite element meshes has been achieved (Homer and Schuh 2010, 2009). In 2D, a single STZ is represented by a node and all the surrounding elements or an element and all the surrounding elements on an irregular triangular mesh, shown in Fig. 3a. This representation ensures that the shapes of potential STZs are roughly equiaxed. Furthermore, in this representation, the STZs comprise more than one single element, so that elements in the mesh will be able to participate in multiple STZs. As illustrated in Fig. 3b, three potential STZs, each of 13 elements, are highlighted on an irregular triangular mesh. At any given time step, the elements in the overlap region (between potential STZs B and C) can participate in either event. Finally, the accuracy of the representation is evaluated by comparing to the Eshelby solution for shearing of a long circular fiber in a matrix (plane strain). The percent error of the calculation relative to the Eshelby solution (based on the total system strain energy) is plotted in Fig. 3c as a function of the size of the STZ relative to the mesh. As the results show, convergence is achieved quite rapidly, with STZs containing 13 or more elements exhibiting about 1.5% error or less (Homer and Schuh 2009).

In 3D, a collection of 20–30 tetrahedral elements that all share one common node provides a consistent approximately spherical STZ, as illustrated in Fig. 2b. In this definition, STZs may overlap. When compared with the Eshelby solution, the quadratic tetrahedral element-based STZs are found to provide higher accuracy with the elastic strain energy having 2% error (Homer and Schuh 2010).

The use of a finite element mesh not only enables a coarse-grained description of STZ as a transient flow defect in metallic glasses but also provides flexibility

for further development to incorporate emerging characteristics of STZs. First, one might define an ensemble of STZs with different characteristic volumes. In principle, this could be achieved based on the local size of the elements included in each potential STZ. In this chapter, a single value of volume is assigned to all the STZs in the mesh, but this value could vary with respect to strain rate (Harris et al. 2016) (see Sect. 3.2). Second, the size of STZ activation volume could be related to the level of glass relaxation and damage (Albaret et al. 2016; Boioli et al. 2017) and loading states (Fusco et al. 2010). Adaptive meshing could be used to capture the dynamic evolution of STZ volumes. Third, the elastic response of the system to the STZ transformation strain requires only the use of a linear elastic finite element solver. The use of finite element mesh and finite element solver enables just about any set of boundary conditions regularly used in finite element analysis to be incorporated into the STZ dynamics framework.

2.2 STZ Activation Rate

To accomplish the dynamics for longer time scale, the STZ dynamics model considers the coarse-grained STZ activation as a transition state between the initial and final equilibrium configurations, as illustrated in Fig. 4a. The stochastic activation of the STZs leads to deformation on longer timescales. The STZs are thermally activated, and the activation rate is proportional to the Boltzmann probability that the system overcomes the activation barrier between the initial and final equilibrium configurations, defined as

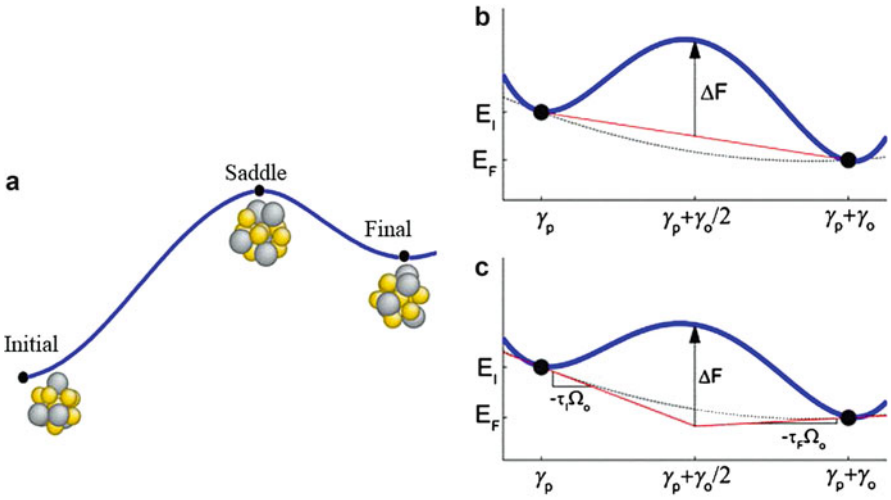

Fig. 4 (**a**) Illustration of the potential energy landscape and the associated STZ configurations at the initial state, saddle point, and final state. (**b**) Illustration of the traditional approach of identifying the activated state of an STZ. (**c**) The energy landscape model proposed by Bulatov and Argon (1994a). (Figure (**b**) and (**c**) reproduced with permission from Homer et al. (2010))

$$\dot{s} = v_o \exp\left(-\frac{\Delta G}{k_B T}\right) \tag{1}$$

where the prefactor ν_o is of the order of the Debye frequency, ΔG is the activation energy barrier, T is the absolute temperature, and k_B is the Boltzmann constant.

In order to calculate the activation energy barrier for a given transition, one must have knowledge of the transition itself. A traditional approach uses the energy change to model the activation energy, ΔG, by adding a barrier of fixed height, ΔF, to the average of E_I and E_F, as illustrated in Fig. 4b. This approach satisfies detailed balance for the reaction because a forward transition traverses the same activated state as the reverse transition.

$$E^I + \Delta G_{I\to F} = E^F + \Delta G_{F\to I} \tag{2}$$

with $\Delta G_{I\to F}=(E^F - E^I)/2 + \Delta F$ and $\Delta G_{F\to I} = (E^I - E^F)/2 + \Delta F$. Unfortunately, this traditional approach of calculating ΔG requires calculation of the energy in the final state, which is computationally expensive for a large number of possible transitions in metallic glasses.

Bulatov and Argon have provided an alternate formulation for ΔG by exploiting the fact that the strain energy associated with shearing an STZ is a quadratic function of the transformation strain γ_0 (Bulatov and Argon 1994a). This quadratic variation in energy, shown as the dashed line in Fig. 4c, can predict the energy in the final state without explicit calculation. Bulatov and Argon simply extrapolate from the initial state, using the slope at that point, to the midpoint of the transition and then add the fixed barrier height, ΔF. The energy difference between the traditional approach and that of Bulatov and Argon is very small (Bulatov and Argon 1994a; Homer et al. 2010). For more detailed explanation, including the requirement of detailed balances, please refer to Homer et al. (2010).

The STZ dynamics framework uses the Bulatov and Argon model and defines the activation energy barrier as

$$\Delta G = \Delta F - \frac{1}{2}\tau \cdot \gamma_o \cdot \Omega_o \tag{3}$$

where the intrinsic barrier height for the reaction, ΔF, is biased by the local shear stress τ, which is obtained by volume averaging the stress over the elements which comprise each potential STZ. The activation volume, $\gamma_0\,\Omega_0$, of the STZ is comprised of the transformation strain increment associated with an STZ transformation, γ_0, and the volume of the STZ, Ω_0. Argon developed a model for ΔF (Argon 1979), given as

$$\Delta F = \left[\frac{7-5v}{30\,(1-v)} - \frac{2\,(1+v)}{9\,(1-v)}\beta^2 + \frac{1}{2\gamma_o}\cdot\frac{\widehat{\tau}}{\mu(T)}\right]\cdot\mu(T)\cdot\gamma_o^2\cdot\Omega_o \tag{4}$$

where the three terms in the brackets define the strain energy associated with shearing of the STZ, the strain energy associated with a temporary dilatation of

the STZ to allow the atoms to rearrange, and the frictional energy associated with the free shearing of the atoms over one another. In the equation of ΔF, ν is Poisson's ratio, β is a ratio of shear to dilatation (usually taken as 1), $\widehat{\tau}$ is the peak interatomic shear resistance between atoms, and μ(T) is the temperature-dependent shear modulus.

The use of Bulatov's and Argon's energy model allows the STZ dynamics model to explore a large number of transitions without calculating the energy of the final state, resulting in significant computational saving. However, a fixed activation energy barrier would be hard to represent the complex non-equilibrium states in metallic glasses that contain many-body interactions and strong disorder. Methods such as the nudged-elastic band (NEB) (Boioli et al. 2017; Xu et al. 2017) or the activation-relaxation technique (ART) (Fan et al. 2014; Malek and Mousseau 2000; Rodney and Schuh 2009) can be used in atomistic simulations to explore the potential energy landscape and find the exact activation energy barrier from any given equilibrium state. Widely distributed activation energies, depending largely on the processing history, are usually obtained (Rodney and Schuh 2009; Rodney et al. 2011). These atomistic energy barrier search methods are computationally intensive and do not readily translate into mesoscale models. The development of activation energy functional based on the atomistic energy barriers, or their associated features, would be beneficial to enrich the STZ dynamics model.

2.2.1 STZ Activation Rate in 2D

The expression for ΔG given in Eq. 3 defines the energy barrier for an STZ to shear in one direction. Since we are interested in calculating the range of barriers associated with shearing an STZ in any direction in space, the shear stress associated with each unique shear direction must be identified and enumerated.

In 2D, the shear stress for each unique shear direction around a circle can be evaluated using a Mohr's circle construct, which gives the shear stress along any direction of the circle as

$$\tau = \tau_{\max} \sin(\theta) \tag{5}$$

where θ is the angle to the stress state with stress τ and which is measured relative to the stress state with the highest principal stress. One can then integrate all shear directions by integrating θ over the interval (0°, 360°). By combining Eqs. 1, 3, and 5, the integral STZ activation rate becomes

$$\dot{s} = \frac{v_o}{2\pi} \cdot \exp\left(-\frac{\Delta F}{k_B T}\right) \cdot \int_0^{2\pi} \exp\left(\frac{\tau_{\max} \cdot \sin(\theta) \cdot \gamma_o \cdot \Omega_o}{2k_B T}\right) d\theta \tag{6}$$

which evaluates to a modified Bessel function of the first kind, of order zero

$$\dot{s} = \frac{v_o}{2\pi} \cdot \exp\left(-\frac{\Delta F}{k_B T}\right) \cdot I_o\left(\frac{\tau_{\max} \cdot \gamma_o \cdot \Omega_o}{2k_B T}\right) \tag{7}$$

This particular form of the STZ activation rate is convenient because the analytical solution gives the rate for shearing an STZ in any direction in two dimensions with only one function evaluation. One can then use this integral rate in the kMC implementation to determine which STZs are likely to be activated.

2.2.2 STZ Activation Rate in 3D

The evaluation of the STZ activation rate in 3D is more complex than the 2D case due to the larger set of possible shear planes and shear directions, as well as the need to only evaluate unique combinations of shear planes and directions. In a generalized form, the integral activation rate can be defined as

$$\dot{s} = v_o \cdot \exp\left(-\frac{\Delta F}{k_B T}\right) \cdot \int_{g \in G}\int\int\int \exp\left(\frac{\tau(\sigma, g) \cdot \gamma_o \cdot \Omega_o}{2k_B T}\right) dg \tag{8}$$

where g is the orientation of any shear plane-shear direction combination belonging to the set G of all unique combinations of shear planes and shear directions. The integral is three dimensional because the specific orientation of a shear plane and shear direction requires three parameters. The shear stress of that orientation g is defined as $\tau(\sigma, g)$ to denote the fact that the triaxial stress state that exists in a given STZ must be transformed by g to obtain the shear stress for that given shear plane and shear direction. No analytical solution to the integral in Eq. 8 could be found. The integral is numerically evaluated and tabulated for rapid recall during the modeling process while maintaining an error less than 0.01%. Due to the complexity of this calculation, the details are not discussed here but are available in (Homer and Schuh 2010).

2.2.3 STZ Activation Rate with Excess Free Volume as a Local State Variable

The initial implementation of the STZ dynamics framework used a fixed ΔF for all STZ events. Potentially important effects related to the glass state, e.g., level of glass relaxation and damage, have not been considered. To solve this limitation, local state variables can be included as part of the energetics that describe STZ activations. The purpose of the state variables is to (1) incorporate local activation energy fluctuation that in broad agreement with the widely distributed activation energies of metallic glass and (2) capture the evolution of the structure beyond the redistribution of stress and strain when an STZ is activated. One could choose from a range of state variables, such as atomic stress and strains, topological or chemical order, free volume, and fictive temperature. In the current STZ dynamics framework, a state variable of "free volume" has been implemented (Li et al. 2013, 2014).

The implementation of free volume is based on Argon's original definition of the STZ, in which he includes free volume as a state variable to capture the structural evolution of the system. Particularly, in our adaptation of the STZ dynamics framework, excess free volume, f_v, is defined as a normalized quantity where $f_v = 0$ corresponds to no excess free volume above the average polyhedral volume in a

dense random hard sphere glass, while $f_v = 1$ is an upper bound corresponding to a state where an STZ can be activated without accumulating any extra free volume.

The excess free volume influences the energy barrier for STZ activation, and the fixed barrier is modified as

$$\Delta F_{STZ}(f_v) = \Delta F_{shear} + \Delta F_{v0} \cdot g_{stz}(f_v) \tag{9}$$

where ΔF_{shear} captures the strain energy associated with shear (not dependent upon excess free volume) and ΔF_{v0} captures the strain energy associated with dilatation and friction of the atoms sliding over each other (dependent upon excess free volume). Equation 9 essentially alters Eq. 4 by recognizing that the first term in the bracket of Eq. 4 is only dependent on shear but not on the magnitude of excess free volume, whereas the last two terms in the bracket of Eq. 4 are dependent upon the magnitude of excess free volume. Furthermore, ΔF_{STZ} is smaller when greater excess free volume exists since the STZ needs to dilate less and the friction will be lowered. This change in the energy is captured by the function g_{stz}, which lowers the activation energy barrier as the excess free volume is increased.

Following a given STZ activation, the excess free volume within the activated STZ is increased since it is believed that the atoms are not able to immediately return to the original magnitude of excess free volume (Li et al. 2013).

In parallel to the activation of STZs, a competing process is introduced as the diffusive rearrangement (and destruction) of excess free volume to capture the effect of structural relaxation in metallic glasses. Following Argon's original model, the rate of diffusive rearrangement is given as

$$\dot{s}_D = (1 - f_v)\, v_D \exp\left(-\frac{\Delta G_D(f_v)}{k_B T}\right) \tag{10}$$

where $\Delta G_D(f_v)$ is the activation energy barrier for diffusive rearrangement, which is dependent upon the current magnitude of excess free volume. Higher excess free volume has a lower energy barrier given that it is farther from the equilibrium state. The quantity $(1–f_v)$ reflects a decrease of available atomic sites for free volume diffusion as f_v increases. The prefactor v_D for the diffusive rearrangements is of the order of the Debye frequency.

It is noteworthy that the implementation of excess free volume and most other state variables at mesoscale remains phenomenological (Rodney et al. 2011). Metallic glasses do not have structural defects found in crystalline materials, such as dislocations and grain boundaries. The definitions of structural defects in disordered materials are not unique and would require some phenomenological presumptions and fitting parameters. A fundamental understanding is still lacking on the dynamics of inherent glassy structure and its connection with the properties of glasses such as aging or rejuvenation (Fan et al. 2017). It remains difficult to develop parameter-free theories based on defects. Atomistic simulations and experimental measurements at microscopic scale would advance the development of "defect"-level theories and their implementation into the mesoscale model.

2.3 Kinetic Monte Carlo Implementation

2.3.1 kMC with STZ Activation

Upon calculation of the STZ activation rate, the kMC algorithm (Voter 2007) is used to evolve a system consisting of an ensemble of STZs. In the system, each STZ may experience different local temperature, stress state, and local state when state variables are incorporated. The kMC algorithm proceeds according to the following steps, which are repeated for every transition:

1. Calculate and form a list of activation rates, $\dot{s}_i$, for each of the $i = 1, \ldots, N$ STZs in the ensemble, based on the current state of the system.
2. Calculate the normalized rate η_i for each STZ via dividing the individual activation rate by the cumulative activation rate, $\eta_i = \dot{s}_i / \dot{s}_T$, for all STZs. The sum over the normalized transition rates is equal to one, i.e., $\sum_i \eta_i = 1$.
3. Generate two random numbers, ξ_1 and ξ_2, uniformly distributed on the interval (0, 1).
4. Update the elapsed system time with the residence time for the current configuration calculated according to $\Delta t = -\ln \xi_1 / \dot{s}_T$.
5. Select a single STZ by first defining the cumulative fraction of STZ rates up to and including the rate of STZ j by $H_j = \sum_{i=1}^{j} \eta_i$, and then use the random number, ξ_2, to find the STZ which satisfies $H_{k-1} < \xi_2 \leq H_k$. When listed in a successive faction, ξ_2 falls on the subinterval in the list of normalized STZ rates, as illustrated in Fig. 5.

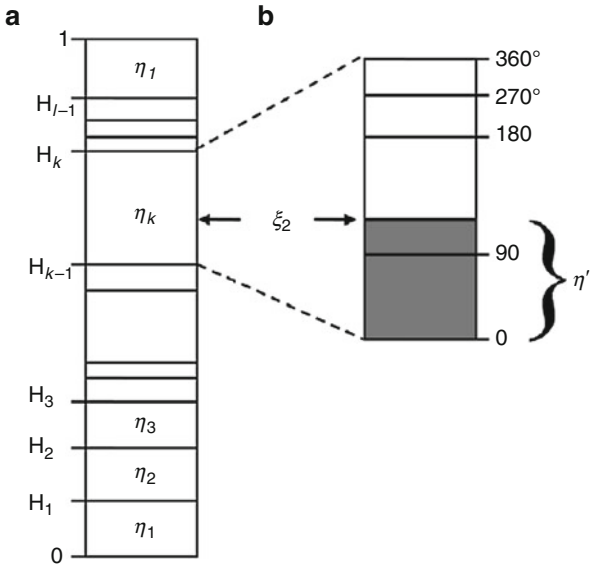

Fig. 5 Schematic of the kinetic Monte Carlo STZ selection procedure. (**a**) How the random number ξ_2 can be used to select a single STZ for activation from a list of normalized individual STZ rates, $\eta_1, \eta_2, \eta_3, \ldots, \eta_i$. (**b**) The determination of the overlap, η', between ξ_2 and η_j, which selects the angle of shear of the STZ. (Figure reproduced with permission from Homer and Schuh (2009))

6. To select the angle at which to shear the STZ, we first define the value $\eta' = \xi_2 - H_{k-1}$, which represents the magnitude by which ξ_2 overlaps the subinterval of the selected STZ, as shown in Fig. 5. The overlap, η', is then used to determine the integration limit and further the angle of shear in real space. The detailed explanation of angle selection can be found in Homer and Schuh (2009) for 2D and in Homer and Schuh (2010) for 3D.
7. Apply the appropriate transformation strain to the selected STZ.
8. Calculate the stress and strain distributions and state-variable evolution resulting from the new configuration.

The kMC algorithm can be repeated for an arbitrary number of STZ operations and is efficient because every iteration guarantees a transition. The stochastic nature of the processes will produce a realistic outcome as long as the rate law of the individual event is correct.

2.3.2 kMC Algorithm with Competing Processes

The kMC algorithm can easily be adapted to incorporate another type of processes competing with STZ activation to evolve the systems. For instance, after incorporating excess free volume as a state variable, a diffusive rearrangement process is introduced in competition with STZ activation. Upon implementation, at a given kMC step, the transition rates of diffusive rearrangement process will be included in addition to STZ activation to make a list of activation rates in Steps 1 and 2 described in Sect. 2.3.1. In Step 5, either diffusive rearrangement or STZ activation is selected, depending on the subinterval ξ_2 falls on in the list of the normalized transition rates. And thus, the two possible processes are exclusive; in each kMC increment, only one of them will be selected. The addition of competing processes is explained in more detail in (Li et al. 2013).

2.4 Summary of STZ Dynamics Framework

The STZ dynamics model simulates the stochastic activation of coarse-grained STZs, their elastic interaction leading to organization and accumulation of STZs forming shear bands at large time and length scales. The application of the modeling framework requires several steps to be followed. First, a 2D or 3D finite element mesh is defined to match the geometry of the model material being simulated. Second, potential STZs are mapped onto the finite element mesh based on the coarse-graining criteria discussed in Sect. 2.1. Third, a set of state variables can be assigned on the finite element mesh, influencing the material model and kMC algorithm, as discussed in Sect. 2.2.3. Fourth, implement the kMC algorithm and repeat the following steps:

1. Determine which STZ should be selected for activation, and which shearing angle should be applied, based on the current system state.

Table 1 Material properties commonly employed by the STZ dynamics framework

Property/variable	Value
Temperature-dependent shear modulus, $\mu(T)$	-0.004 [GPa K^{-1}] $\times$ T + 37 [GPa]
Poisson's ratio, ν	0.352
Debye temperature, θ_D	327 K
Fixed activation energy barrier, $\Delta F(T)$	0.822×10^{-29} [J Pa^{-1}] * μ(T)
STZ activation volume, Ω_o	2.0 nm^3
STZ strain, γ_o	0.1

2. Impose a characteristic transformation strain to the elements belonging to the selected STZ according to the selected shearing angle.
3. Use finite element analysis to determine the response of the system to the imposed transformation strains.
4. Update the current system state, including stress, strain, and any functional material properties, to reflect the response to STZ activation.

These last four steps involving the kMC algorithm are repeated many times in succession to determine the evolution of the system.

The key material properties and simulation variables used by many of the published STZ dynamics papers are listed in Table 1. The attempt frequency ν_o is taken as the Debye frequency, which can be calculated from the Debye temperature θ_D. The variables $\mu(T)$, ν, and θ_D have values for the commonly studied Vitreloy 1 with composition $Zr_{41.2}Ti_{13.8}Cu_{12.5}Ni_{10}Be_{22.5}$ and are obtained from Johnson and Samwer (2005) and Wang et al. (2011b), respectively. Rather than using the complex form of the fixed barrier height in Eq. 4, we reduce ΔF to a simple functional form that is dependent upon the shear modulus. This functional form is also in line with the cooperative shear model proposed by Johnson and Samwer (Johnson and Samwer 2005). The STZ volume is in the range commonly reported in the literature (Zink et al. 2006), and the STZ strain is equal to the commonly accepted value (Schuh et al. 2007). This list of variables is intentionally kept short to simplify the model and obtain an intended response.

3 Applications of STZ Dynamics Model

The STZ dynamics modeling framework provides an opportunity to study many different aspects of metallic glass deformation. Since its original development, the STZ dynamics framework has been adapted for different implementations, including contact mechanics (Packard et al. 2010; Wang et al. 2015) and state-variable free volume evolution (Li et al. 2013; Wang et al. 2015), and for metallic glass matrix composites (Hardin and Homer 2015). In the following section, three applications are chosen to demonstrate:

1. The general behaviors of the STZ dynamics model and the corresponding spatial and temporal correlation of STZ activity that underlies various modes of deformation
2. The physics that control the low-temperature shear banding behavior and how the strain rate influences the shear banding process
3. How nanoindentation can be studied using the STZ dynamics modeling framework to gain insight into nanoscale strengthening in metallic glasses

3.1 General Behaviors and STZ Correlations

Metallic glasses exhibit a great variety of deformation behaviors, depending upon conditions (Schuh et al. 2007). The STZ dynamics model is able to capture the general MG behaviors, showing homogeneous deformation at high temperature and localization deformation into the shear bands at low temperature and high stress. A representative 2D model response is illustrated in Fig. 6a. The 3D model can capture the general behaviors as well (for details, please refer to (Homer and Schuh 2010)).

The model response over a range of conditions is well represented by the deformation map for simulation cells subjected to a range of applied stress at various temperatures. An example of deformation map for the 2D model is displayed in Fig. 6b. The regions of homogeneous deformation and inhomogeneous deformation are shaded. In addition, the steady-state strain rate is measured from each simulation, and contours of constant strain rate are overlaid on the map for rates ranging from 10^{-10} to 1 s^{-1}. The shading inside each data point presents the strain rate sensitivity. At high temperature, as the stress is increased, the strain rate sensitivity decreases from unity toward zero, reflecting a transition from Newtonian flow to non-Newtonian flow. These are the rheological behaviors that metallic glasses exhibit at high temperature. At low temperature, when stress is low, the strain rates are lower than 10^{-10} s^{-1}, which we consider to be "elastic" deformation as the inelastic behaviors would be too slow to be captured in experiments. When the stress is high at low temperature, the strain rate sensitivity is extremely low; in other words, the flow stress is nearly the same for various strain rates. This is a consequence of the formation of shear bands, the details of which will be discussed in Sect. 3.2. The deformation map compares favorably with experimental deformation map, in that it captures the basic features of metallic glass deformation (Schuh et al. 2007).

Underlying the diverse deformation behaviors is the different spatial and temporal correlation of STZ activity. Analysis of the 2D simulations of STZ correlations provides significant insight, represented by the time-dependent radial distribution functions (TRDFs), given as

$$g\,(r,\,j) = \frac{n\,(r,\,j)}{q(r)} \tag{11}$$

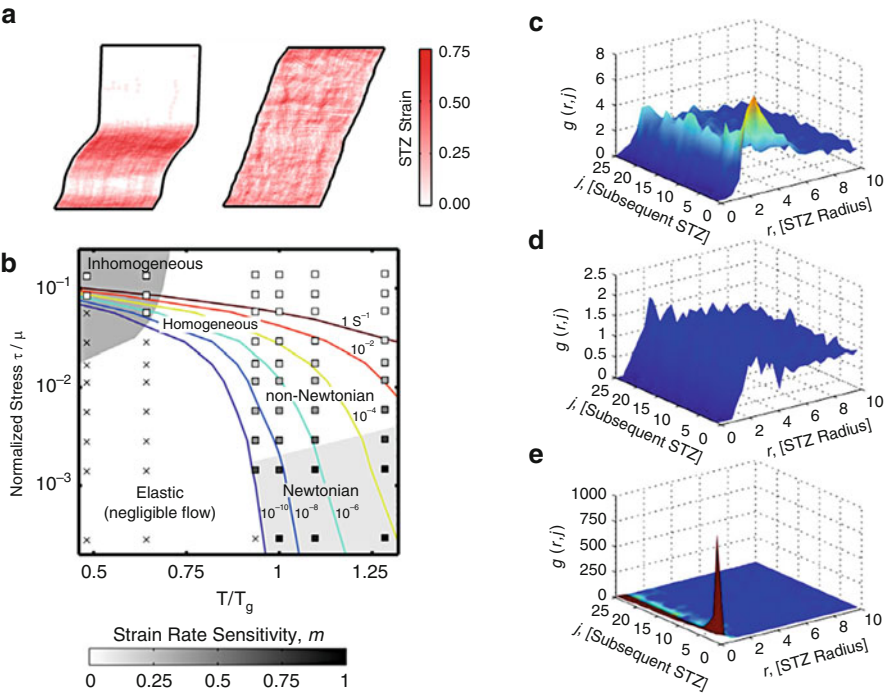

Fig. 6 (**a**) The representative responses of the STZ dynamics model at high and low temperatures in 2D. (**b**) Deformation map for Vitreloy 1 constructed from data obtained by 2D STZ dynamics simulations. The STZ correlation behaviors represented by the TRDFs of STZ activation, where the three behaviors and their corresponding conditions are (**c**) nearest-neighbor STZ activation (high stress and low temperature), (**d**) independent STZ activation (high stress and high temperature), and (**e**) self-STZ activation (low stress and any temperature). (Figures adapted with permission from Homer et al. (2010); Homer and Schuh (2009))

where $n(r, j)$ is constructed by binning the number of sequential activations as a function of radius r and time step j and $q(r)$ is a normalization quantity in each bin with the size dr, defined as

$$q(r) = \begin{cases} 1 & if\ r \leq \frac{1}{2\pi r dr \rho_{STZ}} \\ 2\pi r dr \rho_{STZ} & if\ r > \frac{1}{2\pi r dr \rho_{STZ}} \end{cases} \tag{12}$$

where ρ_{STZ} represents the overall density of STZ activations, i.e., the total number of STZ activations per unit area. The TRDFs' functions indicate the likelihood of shearing an STZ at nearby position and after a certain number of steps relative to a given STZ activation; magnitudes less than 1 are less likely to occur at a given position and time than if it occurs randomly throughout the simulation cell, and magnitudes greater than 1 are more likely to occur at a given position and time than if it occurred randomly throughout the simulation cell.

The TRDF reveals three basic types of behavior that manifest under different combinations of applied stress and temperature as shown in Fig. 6c–e.

- Nearest-neighbor STZ activation, which is observed for simulations at low temperature and high stress in Fig. 6c. This behavior is characterized by an early, broad peak, spanning $r = 1$–5, centered between 2 and 3, indicating the preference for nearest-neighbor activation. This correlated behavior is the source for the shear localization that underlies the macroscopic shear bands observed in experiments.
- Independent STZ activation, which occurs under conditions of high applied stress and high temperatures in Fig. 6d. In this behavior, the TRDF shows no preference for reactivation of STZs atop the first one, since $g(r, j) \sim 0$ at $r < 1$. Furthermore, the tendency for activation of neighboring STZs is lost; there is no longer a discernible peak in the TRDF. There is no noticeable correlation between STZ activations. As expected, the additional thermal energy cancels the effect of stress concentration that might otherwise cause shear localization. Consequently, the uncorrelated STZ activation leads to homogeneous deformation.
- Self-STZ activation, which dominates at low applied stress and any temperature. As illustrated in Fig. 6e, the TRDF exhibits an extremely pronounced and sharp peak at $r = 0$ and for early time ($j < 4$). The spatial extent of the peak is limited to $r \leq 1$, indicating a large preference for a second STZ activation atop the first. The self-STZ activation is linked to the elastic regime. At low temperatures and low stresses, there is an insufficient tendency for a single STZ to trigger nearest-neighbor activations; thus, the most likely response of the system is for each STZ activation to be instantaneously reversed.

The STZ dynamics model can not only capture the MG deformation behaviors at the macroscopic level, matching the experimental behaviors, but also provide insights at a microscopic level on how STZs interact with one another and how their collective operation leads to the deformation on a macroscopic level. These types of studies demonstrate the strength of a mesoscale model that successfully coarse-grains a process and determine the transitions that control the evolution of the system.

3.2 Shear Banding Process at Low Temperature

Among the diverse deformation modes exhibited by metallic glasses, the low-temperature shear banding behavior is of the greatest interest. The limited ductility due to the formation of a catastrophic shear band before failure is the primary issue that hinders the wide application of metallic glass as a structural material (Greer et al. 2013; Schuh et al. 2007). The STZ dynamics model can provide modeling details into the formation of the shear band, which remain unresolved due to the difficulty in accessing the appropriate time and length scales experimentally.

One can study the shear localization process into one shear band in detail (Homer 2014). Snapshots of a 3D simulation cell subject to constant strain rate, uniaxial tension test are shown in Fig. 7. Examination of the simulation results reveals five different stages in the microscopic processes:

(I) Purely elastic, with no STZ activity
(II) STZ clustering, where correlated STZ activations lead to the formation of clusters
(III) Growth following nucleation of a shear band, where all STZ activity transitions from being distributed throughout the simulation cell to being concentrated in the shear band
(IV) Relaxation thickening, which is manifest by the continued thickening of the shear band while the stress is still dropping even after it has propagated across the simulation cell
(V) Flow thickening, which is indicated by the continued thickening of a single shear band at a constant flow stress

Most of the plastic strain is accumulated during the sliding process, indicating that nucleation and initial propagation of a shear band are very brief. Analysis of a thermodynamic model also suggests a specific yield stress that is required to nucleate a shear band, after which the shear band is allowed to grow unconstrained.

In addition to the individual shear band, the STZ dynamics model has been adapted to investigate a collection of shear band events, which leads to the transition in flow serration in the inhomogeneous deformation regime. An interesting deformation phenomenon associated with metallic glass is that the shear band density and degree of flow serration are highly strain rate dependent, though the yield point of these materials is often independent of strain rate for rates up to $10^2 \sim 10^3$ s^{-1} (Schuh et al. 2007, 2004). Low strain rates are characterized by strongly serrated flow, meaning that strain accumulates in the material in temporal bursts accompanied by relaxation stress drops resulting in a jagged stress-strain curve (Dalla Torre et al. 2010; Song et al. 2008). Higher strain rates are characterized by moderately serrated flow, and very high strain rates have little or no flow serration. The mechanisms that underlie the transition are hypothesized to be the competition between shear band nucleation and propagation (Schuh et al. 2004).

The STZ dynamics framework exhibits a yield point that is inherently rate dependent. To correct for this and make the yield point rate independent, the STZ dynamics model is extended to incorporate a strain-rate-dependent STZ volume and activation energy, given by the following log-linear forms:

$$\begin{aligned} \Omega_0 &= -0.2\log_{10}\dot{\varepsilon} + 1.6 \quad [\mathrm{nm}^3] \\ \Delta F &= -0.12\log_{10}\dot{\varepsilon} + 1.07945 \quad [\mathrm{eV}] \end{aligned} \tag{13}$$

This parameterization of STZ volume and STZ energy barrier as a function of strain rate is not unique but aims to capture physical mechanisms of STZs (Dubach et al. 2009; Harris et al. 2016). The physical origin of the strain rate dependence

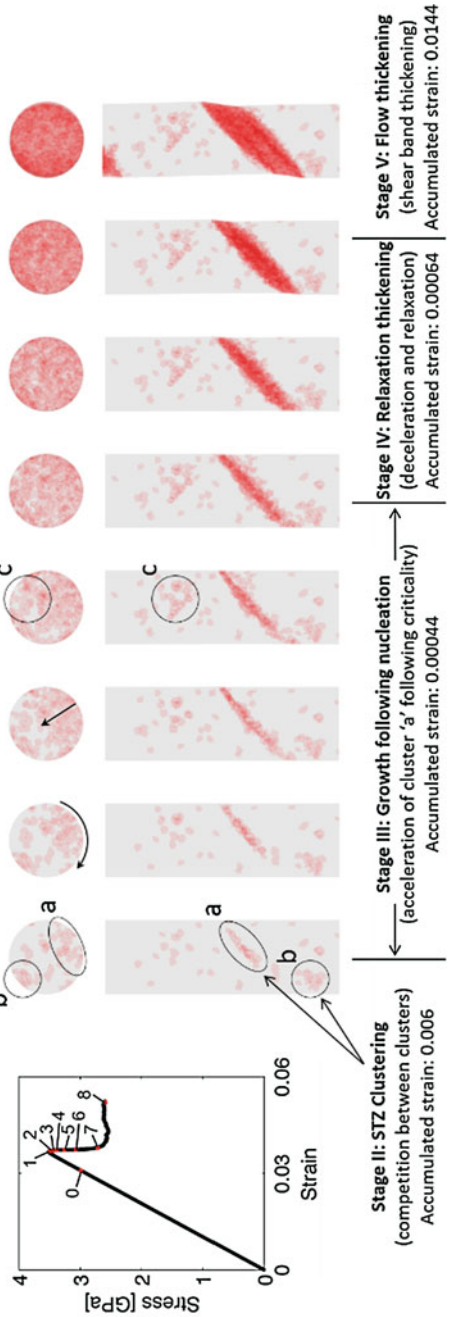

Fig. 7 Shear localization process into one shear band. Numbered snapshots of the model metallic glass at various times during a constant strain rate, uniaxial tensile simulation. Each snapshot includes a semitransparent top and side view of the simulation cell. The evolution of the shear band is divided into four different stages following the initial elastic response. (Figure reproduced with the permission from Homer (2014))

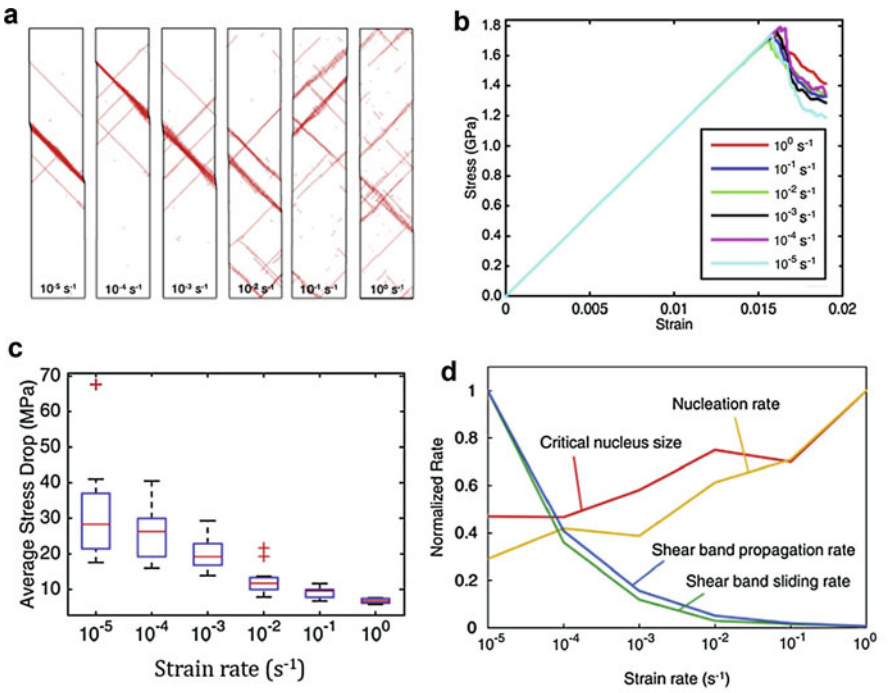

Fig. 8 (**a**) Example simulations at various strain rates. Note the clear trend of increased shear band density with strain rate, and the increased appearance of free STZs at higher strain rates. (**b**) Stress-strain curves for the six simulations shown in (**a**). (**c**) Box plot of the average stress drop magnitude in each simulation, arranged by strain rate. (**d**) The comparison of median values of the normalized shear band nucleation rate (yellow), shear band propagation rate (blue), and shear band sliding rate (green). (Figure reproduced with permission from Harris et al. (2016))

remains an open question, possibly contributing to the time-dependent structural relaxation (Dubach et al. 2009) or a kinetic feature of the atomic motions associated with an STZ.

A transition of shear band density and morphology is captured by the model with increasing strain rate from 10^{-5} s^{-1} to 1 s^{-1}. Figure 8a shows a group of six simulations, one from each strain rate studied, with increasing strain rate from left to right. Each simulation is at the final strain value of 1.9%. In general, low strain rates result in fewer, more dominant shear bands, with very few free STZs scattered outside the bands, while high strain rates feature larger numbers of less dominant shear bands, with many free STZs randomly scattered outside the bands. The corresponding stress-strain curves for these six simulations are displayed in Fig. 8b, showing a tightly grouped yield strength around 1.72 GPa. While the yield strengths are similar, low strain rates tend to relax more quickly after yield and have a lower flow stress than high strain rates. Examination of the flow serration regarding stress drop after yielding shows a negative correlation with strain rate (Fig. 8c). This

is in line with the experimental observations: strongly serrated flow at low strain rate and moderately serrated flow at higher strain rate.

Further study of shear band nucleation rates, propagation rates, and sliding rates in each simulation shows a transition from propagation-dominated shear banding at low strain rates to nucleation-dominated shear banding at high strain rates. A summary of the different statistics and their strain rate dependence is illustrated in Fig. 8d, where each rate has been scaled so they can be compared side by side. The underlying cause for the flow transition is hypothesized to be a strain-rate-dependent critical shear band nucleus size that increases with increasing strain rate (Harris et al. 2016). This is best illustrated by examining the stages of shear banding (ref. to Fig. 7). In the nucleation stage (II), STZs appear and begin to cluster into shear band nuclei, which grow and proliferate in the absence of a dominant shear band. If the strain rate is low, then a small critical nucleus size means that the growth stage (III) is reached quickly, and one shear band rapidly propagates across the sample and begins to dominate all plasticity in the sample. Then, in the sliding stage (IV and V), additional plasticity is concentrated in bursts on that dominant band. If instead the strain rate is high, then a large critical nucleus size means that the growth stage (III) is delayed, or skipped entirely, and plasticity continues to be accommodated by nucleation of additional shear band nuclei in the nucleation stage (II). Then sliding stage (IV and V) occurs more gradually as shear band nuclei begin to intersect each other, and plasticity remains relatively diffuse.

In essence, the STZ dynamics model provides insight into the shear banding process, contributing toward a better picture incorporating both kinetic and thermodynamic nucleation criteria of shear band formation. These types of studies demonstrate the strength of mesoscale models in elucidating the micromechanics behind the macroscopic process. Some of these features would be difficult to observe by other techniques.

3.3 Nanoscale Strengthening Subjected to Cyclic Nanoindentation

Metallic glasses exhibit a broad range of interesting phenomena due to the inherently complex non-equilibrium states, one of which is that they can exhibit nanoscale strengthening subjected to cyclic nanoindentation in the elastic regime. This has been demonstrated in nanoindentation experiment, showing a statistical increase in strength as a result of cyclic loading at a magnitude before the first significant plastic event (e.g., shear band), signified by a pop-in on the load-displacement curve (Packard et al. 2010, 2008). Interestingly, the cyclic strengthening can only occur if the cycling is of a sufficient magnitude, if the indenter is actually cycled (holding a constant load of equal magnitude and time does not lead to strengthening), and the strengthening saturates after a finite amount of cycles.

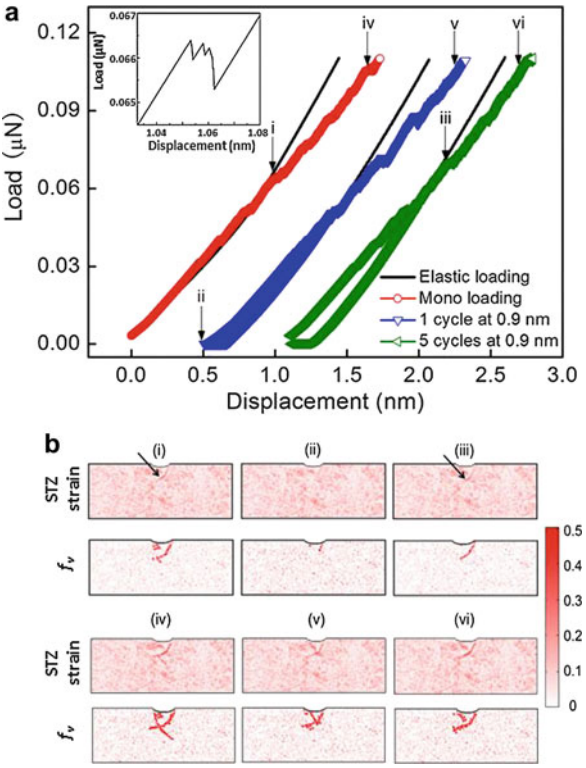

Fig. 9 Simulated nanoindentation results for various loading conditions. (**a**) Load-displacement curves for the monotonic loading, one-cycle and five-cycle loading with the cyclic depth of 0.9 nm. Vertical arrows indicate the points: (i) at the yield of the monotonic loading; (ii) at the reload after the first cycle; (iii) at yield after the five-cycle loading; and (iv), (v), and (vi) at a post-yield load of 0.1 μN for the three loading conditions. The origin of the one-cycle and five-cycle loading curves are shifted for a clear view. The inset shows an enlarged view of load drops around (i). (**b**) The snapshots display the spatial distribution of STZ strain and excess free volume f_v at points (i–vi). Black arrows denote the STZ strain accumulation at (i) and (iii). (Figure reproduced with permission from Wang et al. (2015))

To elucidate the underlying mechanisms that cause the strengthening, the STZ dynamics framework is adapted by including contact mechanics in the finite element analysis solver (Packard et al. 2011, 2010). Furthermore, the model incorporates excess free volume as a state variable, to study the interplay of glass deformation and structural evolution under cyclic indentation tests at an experimentally relevant time scale (Wang et al. 2015).

Results from simulations under various loading conditions are illustrated in Fig. 9. For a clear view, the origins of the load-displacement curves with cyclic loading are shifted to the right. In Fig. 9a, from left to right, the three curves represent the monotonic loading, one-cycle and five-cycle loadings with the cyclic depth of 0.9 nm, respectively. The yield point of each test is indicated by an

arrow, identified by an applicable deviation from the elastic response. The yield load increases with the number of cycles, and after five cycles, it is ∼ 10% higher than that of the monotonic response, which is consistent with the nanoscale cyclic strengthening observed experimentally. Additionally, the snapshots of the spatial distributions of STZ strain and excess free volume at several critical moments are displayed in Fig. 9b. The accumulation of excess free volume can be clearly observed at (i) and (iii), indicating extensive STZ activity prior to the yield point. The cyclic loading can lead to structural change reflected by the annihilation of excess free volume. In a comparison of excess free volume distribution at (i) with (iii), the cluster on the top left in (i) almost disappears after five cycles in (iii). This decrease of excess free volume after cyclic loading gives rise to the mechanical strengthening as a consequence of removal of mechanically weak sites.

The nanoindentation simulation has further been used to detect the cause of nanoscale strengthening subject to cyclic loading. For instance, Fig. 10a displays the cumulative distribution of the yield loads at ten different indentation locations for monotonic and cyclic loadings after one, three, and five cycles, at the cyclic depths of 0.9 nm. Notably, there exists a large distribution of yield loads for monotonic loading, e.g., the minimum yield load is about half of the maximum one. Further, as the number of cycles increases, the distribution curves become sharper and shift to the right particularly at the lower tail, indicating that the "weak" samples are strengthened during cyclic loading. Such effect could be contributed to the removal of the residual stress (Wang et al. 2011a), structural relaxation (Pan et al. 2009), and the arrest of the shear band (Yang et al. 2006). With excess free volume as a state variable, the STZ dynamics simulations demonstrate that the strengthening is directly related to the decrease of large excess free volume sites. When the loading cycles increase from 0 (i.e., monotonic) to 5, the excess free volume is reduced progressively, signified by a left shift of the distribution curves shown in Fig. 10b.

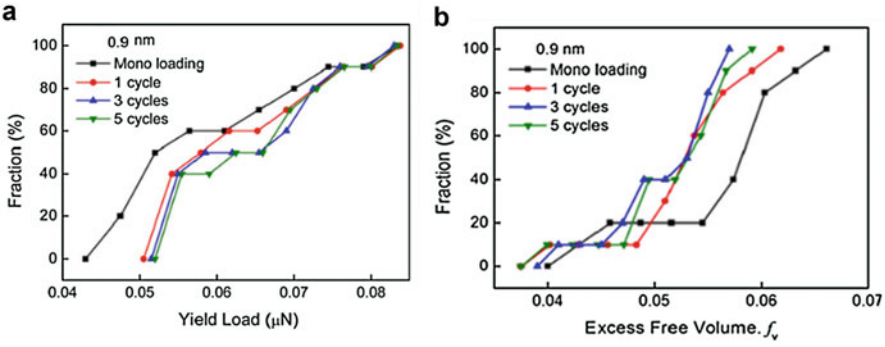

Fig. 10 (**a**) Cumulative distributions of the yield loads for monotonic loading, and various cyclic loadings after one, three, and five cycles at the cyclic depth of 0.9 nm. (**b**) Cumulative distribution curves of the excess free volume f_v in a selected region for monotonic loading and various cyclic loadings after one, three, and five cycles at the depth of 0.9 nm. (Figure adapted with permission from Wang et al. (2015))

The reduction of excess free volume has been ascribed to the observed cyclic strengthening, since it results in a reduced rate of microplastic events by increasing STZ activation energy. Additionally, the left shift becomes less pronounced after one cycle and saturates after five cycles, which is consistent with the saturation of the strengthening effect. Overall, the STZ dynamics simulations indicate that the energetics and timescales of STZ activity are plausible as a mechanism to cause structural evolution that is consistent with nanoscale strengthening.

The application of a mesoscale technique to investigate the nanomechanics of experiments indicates the strong potential to elucidate phenomena that are difficult to measure by experimental techniques.

4 Conclusions and Outlooks

The STZ dynamics model, combining a coarse-grained approach and the kMC algorithm, provides a useful framework to investigate the deformation behaviors of metallic glasses. On the one hand, the coarse-graining enables collections of atoms, or STZs, to be tracked; on the other hand, the kMC algorithm allows the stochastic activation of these STZs based on the energetics of the system. The combination of these two features enables the simulation of deformation behavior at larger time and length scales while preserving a microscopic view of the processes that dominate deformation.

The STZ dynamics model has been used to investigate the deformation behaviors of metallic glasses in a variety of conditions. The modeling technique captures the overall deformation behaviors expected of metallic glasses and the underlying spatial and temporal correlations of STZs that contribute to different deformation modes. The mesoscale model provides details into the formation of individual shear band and the collection of shear band events which leads to the transition of flow serration in the inhomogeneous deformation regime. Insights into nanoindentation experiments are possible through the contact mechanics adaptions. The interplay of deformation and structural evolution is accessed via the incorporation of a free volume state variable.

The STZ dynamics framework will continue to be useful in the investigation of the mechanical behaviors of metallic glasses. Many challenges remain for further development, which includes, among others:

- *Activation energy functional:* The development and implementation of activation energy functionals that more accurately capture the nature and variability of disordered glassy structure and the structural dynamics of metallic glasses.
- *Failure mechanisms:* The failure of metallic glasses involves the strain softening, adiabatic heating, cavitation, and crack formation in shear bands. One could incorporate heat and mass transfer constitutive relations that are capture conditions leading up to failure. One could also include an additional stochastic process for cavitation that precedes crack formation. Finally, once a crack is

initiated, one could model the crack propagation using standard finite element techniques.

- *Adaptive coarse-graining:* Since the scales of STZs and shear bands are different, one could use adaptive meshing to optimize the simulations. Depending on the nature of what is happening, one could coarsen or refine a mesh. For example, after a shear band appears, one could deal with groups of STZs instead of dealing with individual STZs. Mesh refinement/remeshing may be geometrically challenging but can be handled in practice with the use of advanced adaptive meshing algorithms available in finite element packages. Mesh coarsening could also be handled but would require the knowledge of the dynamic evolution of STZ activation volume.
- *Large-scale simulations:* While powerful, current implementations of the STZ dynamics framework are limited in their ability to simulate large structure. A parallel, distributed memory implementation of the STZ dynamics modeling would significantly increase the size of systems that can be examined by the technique. In particular, a different implementation might allow the use of high-performance computing systems. Large-scale simulations would help answer questions about shear banding phenomena beyond the initial stage of shear band formation, which is essential to directly connect with metallic glass toughness and failure at the macroscopic scale.

Acknowledgments LL was supported by the US Department of Energy, Office of Science, Basic Energy Sciences (BES), by award no. DE-SC0016164. ERH was supported by the National Science Foundation under award no. DMR-1507095.

References

Albaret T, Tanguy A, Boioli F, Rodney D (2016) Mapping between atomistic simulations and Eshelby inclusions in the shear deformation of an amorphous silicon model. Phys Rev E 93:053002

Argon AS (1979) Plastic deformation in metallic glasses. Acta Metall 27:47–58

Baret J-C, Vandembroucq D, Roux S (2002) Extremal model for amorphous media plasticity. Phys Rev Lett 89:195506

Boioli F, Albaret T, Rodney D (2017) Shear transformation distribution and activation in glasses at the atomic scale. Phys Rev E 95:033005

Bulatov VV, Argon AS (1994a) A stochastic model for continuum elasto-plastic behavior. I. Numerical approach and strain localization. Model Simul Mater Sci Eng 2:167

Bulatov VV, Argon AS (1994b) A stochastic model for continuum elasto-plastic behavior. II. A study of the glass transition and structural relaxation. Model Simul Mater Sci Eng 2:185

Bulatov VV, Argon AS (1994c) A stochastic model for continuum elasto-plastic behavior. III. Plasticity in ordered versus disordered solids. Model Simul Mater Sci Eng 2:203

Cheng YQ, Ma E (2011) Atomic-level structure and structure–property relationship in metallic glasses. Prog Mater Sci 56:379–473

Dahmen KA, Ben-Zion Y, Uhl JT (2009) Micromechanical model for deformation in solids with universal predictions for stress-strain curves and slip avalanches. Phys Rev Lett 102:175501

Dalla Torre FH, Klaumünzer D, Maaß R, Löffler JF (2010) Stick–slip behavior of serrated flow during inhomogeneous deformation of bulk metallic glasses. Acta Mater 58:3742–3750

Ding J, Patinet S, Falk ML, Cheng Y, Ma E (2014) Soft spots and their structural signature in a metallic glass. Proc Natl Acad Sci 111:14052–14056
Dubach A, Dalla Torre FH, Löffler JF (2009) Constitutive model for inhomogeneous flow in bulk metallic glasses. Acta Mater 57:881–892
Eshelby JD (1957) The determination of the elastic field of an ellipsoidal inclusion, and related problems. Proc R Soc Lond A Math Phys Sci 241:376
Falk ML, Maloney CE (2010) Simulating the mechanical response of amorphous solids using atomistic methods. Eur Phys J B 75:405–413
Fan Y, Iwashita T, Egami T (2014) How thermally activated deformation starts in metallic glass. Nat Commun 5:5083
Fan Y, Iwashita T, Egami T (2017) Energy landscape-driven non-equilibrium evolution of inherent structure in disordered material. Nat Commun 8:15417
Fusco C, Albaret T, Tanguy A (2010) Role of local order in the small-scale plasticity of model amorphous materials. Phys Rev E 82:066116
Greer AL, Cheng YQ, Ma E (2013) Shear bands in metallic glasses. Mater Sci Eng 74:71–132
Hardin TJ, Homer ER (2015) Microstructural factors of strain delocalization in model metallic glass matrix composites. Acta Mater 83:203–215
Harris MB, Watts LS, Homer ER (2016) Competition between shear band nucleation and propagation across rate-dependent flow transitions in a model metallic glass. Acta Mater 111:273–282
Homer ER (2014) Examining the initial stages of shear localization in amorphous metals. Acta Mater 63:44–53
Homer ER, Schuh CA (2009) Mesoscale modeling of amorphous metals by shear transformation zone dynamics. Acta Mater 57:2823–2833
Homer ER, Schuh CA (2010) Three-dimensional shear transformation zone dynamics model for amorphous metals. Model Simul Mater Sci Eng 18:065009
Homer ER, Rodney D, Schuh CA (2010) Kinetic Monte Carlo study of activated states and correlated shear-transformation-zone activity during the deformation of an amorphous metal. Phys Rev B 81:064204
Hufnagel TC, Schuh CA, Falk ML (2016) Deformation of metallic glasses: recent developments in theory, simulations, and experiments. Acta Mater 109:375–393
Hwang J, Melgarejo ZH, Kalay YE, Kalay I, Kramer MJ, Stone DS, Voyles PM (2012) Nanoscale structure and structural relaxation in $Zr_{50}Cu_{45}Al_5$ Bulk Metallic Glass. Phys Rev Lett 108:195505
Johnson WL, Samwer K (2005) A universal criterion for plastic yielding of metallic glasses with a $(T/T_g)^{2/3}$ temperature dependence. Phys Rev Lett 95:195501
Li L, Homer ER, Schuh CA (2013) Shear transformation zone dynamics model for metallic glasses incorporating free volume as a state variable. Acta Mater 61:3347–3359
Li L, Wang N, Yan F (2014) Transient response in metallic glass deformation: a study based on shear transformation zone dynamics simulations. Scr Mater 80:25–28
Liu YH et al (2011) Characterization of nanoscale mechanical heterogeneity in a metallic glass by dynamic force microscopy. Phys Rev Lett 106:125504
Ma E, Ding J (2016) Tailoring structural inhomogeneities in metallic glasses to enable tensile ductility at room temperature. Mater Today 19:568–579
Ma E, Zhang Z (2010) Reflections from the glass maze. Nat Mater 10:10
Malek R, Mousseau N (2000) Dynamics of Lennard-Jones clusters: a characterization of the activation-relaxation technique. Phys Rev E 62:7723–7728
Maloney C, Lemaître A (2004) Universal breakdown of elasticity at the onset of material failure. Phys Rev Lett 93:195501
Maloney CE, Lemaître A (2006) Amorphous systems in athermal, quasistatic shear. Phys Rev E 74:016118
Packard CE, Witmer LM, Schuh CA (2008) Hardening of a metallic glass during cyclic loading in the elastic range. Appl Phys Lett 92:171911

Packard CE, Homer ER, Al-Aqeeli N, Schuh CA (2010) Cyclic hardening of metallic glasses under Hertzian contacts: Experiments and STZ dynamics simulations. Philos Mag 90: 1373–1390

Packard CE, Franke O, Homer ER, Schuh CA (2011) Nanoscale strength distribution in amorphous versus crystalline metals. J Mater Res 25:2251–2263

Pan D, Yokoyama Y, Fujita T, Liu YH, Kohara S, Inoue A, Chen MW (2009) Correlation between structural relaxation and shear transformation zone volume of a bulk metallic glass. Appl Phys Lett 95:141909

Picard G, Ajdari A, Bocquet L, Lequeux F (2002) Simple model for heterogeneous flows of yield stress fluids. Phys Rev E 66:051501

Rodney D, Schuh C (2009) Distribution of thermally activated plastic events in a flowing glass. Phys Rev Lett 102:235503

Rodney D, Tanguy A, Vandembroucq D (2011) Modeling the mechanics of amorphous solids at different length scale and time scale. Model Simul Mater Sci Eng 19:083001

Schuh CA, Lund AC, Nieh TG (2004) New regime of homogeneous flow in the deformation map of metallic glasses: elevated temperature nanoindentation experiments and mechanistic modeling. Acta Mater 52:5879–5891

Schuh CA, Hufnagel TC, Ramamurty U (2007) Mechanical behavior of amorphous alloys. Acta Mater 55:4067–4109

Song SX, Bei H, Wadsworth J, Nieh TG (2008) Flow serration in a Zr-based bulk metallic glass in compression at low strain rates. Intermetallics 16:813–818

Şopu D, Stukowski A, Stoica M, Scudino S (2017) Atomic-level processes of shear band nucleation in metallic glasses. Phys Rev Lett 119:195503

Spaepen F (1977) A microscopic mechanism for steady state inhomogeneous flow in metallic glasses. Acta Metall 25:407–415

Srolovitz D, Vitek V, Egami T (1983) An atomistic study of deformation of amorphous metals. Acta Metall 31:335–352

Su C, Anand L (2006) Plane strain indentation of a Zr-based metallic glass: experiments and numerical simulation. Acta Mater 54:179–189

Tsai P, Kranjc K, Flores KM (2017) Hierarchical heterogeneity and an elastic microstructure observed in a metallic glass alloy. Acta Mater 139:11–20

Voter AF (2007) Introduction to the kinetic Monte Carlo method. In: Sickafus KE, Kotomin EA, Uberuaga BP (eds) Radiation effects in solids. Springer, Dordrecht, pp 1–23

Wang L, Bei H, Gao YF, Lu ZP, Nieh TG (2011a) Effect of residual stresses on the hardness of bulk metallic glasses. Acta Mater 59:2858–2864

Wang N, Ding J, Yan F, Asta M, Ritchie RO, Li L (2018) Spatial correlation of elastic heterogeneity tunes the deformation behavior of metallic glasses. npj Comput Mater 4:19

Wang N, Yan F, Li L (2015) Mesoscopic examination of cyclic hardening in metallic glass. J Non-Cryst Solids 428:146–150

Wang WH, Wen P, Zhao DQ, Pan MX, Wang RJ (2011b) Relationship between glass transition temperature and Debye temperature in bulk metallic glasses. J Mater Res 18:2747–2751

Xu B, Falk M, Li J, Kong L (2017) Strain-dependent activation energy of shear transformation in metallic glasses. Phys Rev B 95:144201

Yang B, Riester L, Nieh TG (2006) Strain hardening and recovery in a bulk metallic glass under nanoindentation. Scr Mater 54:1277–1280

Zhao P, Li J, Wang Y (2013) Heterogeneously randomized STZ model of metallic glasses: softening and extreme value statistics during deformation. Int J Plast 40:1–22

Zink M, Samwer K, Johnson WL, Mayr SG (2006) Plastic deformation of metallic glasses: size of shear transformation zones from molecular dynamics simulations. Phys Rev B 73:172203